

Thermodynamic and kinetic properties of the Lithium–Silver system

Jeremiah Thomas, Sessa Sai Behara, and Anton Van der Ven*

Materials Department, University of California Santa Barbara, Santa Barbara, California 93106, United States

E-mail: avdv@ucsb.edu

Abstract

A carbon-silver anode has recently been shown to suppress dendrite formation in all-solid-state lithium-ion batteries. The role that silver plays in enabling the reversible deposition and stripping of lithium remains unknown. Furthermore, very little is known about the thermodynamic and kinetic properties of $\text{Li}_x\text{Ag}_{1-x}$ alloys. Here we report on an in-depth first-principles study of phase stability and diffusion mechanisms in the Li–Ag alloy system. We identify two new intermetallic phases that are predicted to be stable in Li-rich $\text{Li}_x\text{Ag}_{1-x}$ alloys having stoichiometries of Li_3Ag and $\text{Li}_{11}\text{Ag}_2$. Our calculations also show that the peculiar and highly anharmonic energy surface of pure Li along the Bain and Burgers paths persists upon addition of Ag to BCC Li. This has important implications for room temperature phase stability and mechanical properties. We have also performed a systematic study of diffusion mechanisms in the $\text{Li}_x\text{Ag}_{1-x}$ alloy system as a function of alloy concentration x . Diffusion in alloys and intermetallics is mediated by vacancies. High vacancy formation energies are predicted in the $\text{Li}_x\text{Ag}_{1-x}$ alloy, especially in Ag-rich FCC solid solutions. Complex diffusion mechanisms are identified in the B2 and γ -brass intermetallic phases that include two-atom hops and second nearest neighbor hops. The migration barriers are found to decrease with increasing Li concentration, with predictions of exceptionally low migration barriers of 0.1 eV in the D0_3 Li_3Ag phase.

1 Introduction

All-solid-state Li batteries promise significant increases in energy density relative to commercial Li-ion batteries.¹ One potential advantage of an all-solid-state battery over those that rely on liquid electrolytes is that the structural rigidity of a solid electrolyte should enable the replacement of graphite anodes with more energy dense lithium metal. Unfortunately, it has proven difficult to control the morphological evolution of the lithium metal deposited at the anode current collector during charging and discharging of solid-state batteries.^{2–8} Dendrites that can penetrate the ceramic electrolyte form during rapid lithium plating, while stripping can result in the formation of voids and dead lithium. The pioneering work of Lee et al.⁹ demonstrated the beneficial role of a composite interlayer of silver and carbon in fostering the uniform plating and stripping of lithium. While of tremendous promise, Ag is costly and alternative strategies of controlling morphological evolution at the anode of solid state batteries are desired. Nevertheless, the establishment of a mechanistic understanding of the precise roles that Ag and C and their composite micro/nano structure play during lithium plating and stripping will serve as an invaluable guide to identifying alternative solutions to control morphological evolution at the anode. But before this is even possible, it is necessary to develop an understanding of the fundamental thermodynamic and kinetic properties of the Li–Ag alloy system since there is experimental evidence that Li reacts

with Ag during deposition.¹⁰

Many basic properties of the Li–Ag alloy system remain poorly characterized and understood. The compositions and crystal structures of several intermetallic phases in the lithium–silver binary system are still unknown. The most recent phase diagrams report a Ag-rich FCC solid solution, a Li-rich BCC solid solution, and four intermetallic phases consisting of the B2 LiAg phase and three γ -brass phases that have structural similarities with BCC.¹¹ The stability range of the silver-rich FCC solid solution varies widely between different reports as do the compositions of the γ phases.^{11–14} Of these, the γ_3 phase is the most studied, having an ordering reported to be similar to the slightly disordered Cu_5Zn_8 .^{15,16} In the experimental literature, its composition is most commonly reported as Li_9Ag_4 . The remaining γ phases have proven difficult to synthesize and characterize, and their stability has been called into question by recent computational work.^{17,18} A further peculiarity is the phase transformation from BCC-based B2 LiAg to an FCC-based UPb structure reported by Pavlyuk et al.¹⁹

Even less is known about diffusion within the solid solutions and ordered intermetallic phases of the Li–Ag alloy system. Substitutional diffusion in metallic alloys is generally mediated by entropically stabilized vacancies, which are present at very dilute concentrations.^{20–23} Diffusion in intermetallic compounds can be especially complex as individual hops can disrupt the thermodynamically preferred long-range order of the compound.^{23–27} Multi-atom hop cycles that occur in rapid succession are a common mechanism that preserves long-range order.^{24–26,28} Furthermore, vacancies in intermetallic compounds tend to prefer one sublattice over others, leading to correlated diffusion.^{23,29}

Additional ambiguities in the Li–Ag alloy system arise from the peculiar energy surface of pure lithium along transformation pathways between different crystal structures.^{30,31} For example, the energy of lithium along the Bain and Burgers paths, which connect BCC to FCC and BCC to HCP, respectively, is unusually flat, exhibiting an extreme form of anharmonicity.^{31,32} Furthermore, the energy of BCC lithium is predicted to differ from that of close-packed phases

such FCC, HCP, DHCP, and 9R lithium by less than 1 meV/atom.^{30,31} The unusual anharmonic energy surface of lithium at zero kelvin suggests that the room temperature BCC crystal structure is entropically stabilized, likely making its mechanical properties strongly dependent on temperature. How alloying elements such as Ag affect the anharmonic energy surface of pure lithium remains unknown. The manner in which Ag affects the lithium energy surface will have consequences for the mechanical properties of the alloy.

In this article, we report on an in-depth first-principles study of phase stability and diffusion in the lithium–silver binary system. We systematically enumerate different Li–Ag arrangements over the sites of the family of γ -brass phases and identify a new ground state with a stoichiometry of $\text{Li}_{11}\text{Ag}_2$ that coincides with the composition of γ_1 reported in the literature. We calculate the energy surface of Li–Ag alloys along Bain and Burgers paths and find that Li-rich alloys exhibit a high degree of anharmonicity, with the BCC, FCC, and HCP crystal structures remaining highly degenerate up to a Ag atom fraction of 0.25. Using a first-principles statistical mechanics approach that relies on cluster expansion surrogate models and Monte Carlo simulations, we calculate the room-temperature equilibrium voltage curve. We also perform a systematic study of migration barriers in the different phases of the Li–Ag binary system, accounting for the effects of solid solution and anti-site disorder.

While diffusion barriers are low throughout this system, vacancy formation energies are large and positive, especially in FCC-based phases. Unusual hop mechanisms are predicted in the B2 LiAg phase, including a 2-atom hop mechanism that is essential to mediate the migration of Li to the Ag sublattice. Exceptionally low migration barriers are predicted in the Li-rich phases, with barriers as low as 0.1 eV. Our comprehensive study of migration barriers suggests that diffusion in the Ag-rich FCC solid solution is significantly slower than in the Li-rich γ and BCC phases, which has important consequences when Li reacts with Ag.

2 Methods

We used density functional theory (DFT) within the PBE approximation as implemented in the Vienna Ab-initio Simulation Package (VASP) to optimize structures and to calculate formation energies and diffusion barriers in the lithium-silver system.^{33–36} All calculations were performed with the Li_{sv} and Ag PAW pseudopotentials provided with VASP.³⁷ These pseudopotentials treat the Li 1s and 2s and the Ag 4d and 5s electrons as valence electrons. We optimized lattice parameters and atomic positions in all structures with an energy cutoff of 650 eV and a Γ -centered k -point mesh with minimum spacing $2\pi/64 \text{ \AA}^{-1}$ in order to get a converged accuracy of 1 meV/atom. Relaxations were performed with Gaussian smearing with a smearing width of 0.02 eV and final energy calculations were performed with the tetrahedron method with Blöchl corrections.³⁷ The stopping criteria for geometric optimization was 10^{-5} eV for the electronic steps and 0.02 eV/Å for the forces during the ionic steps.

In order to calculate energy barriers for diffusion, we performed nudged elastic band (NEB) calculations with 5 images using the climbing image method as implemented in the Transition State Theory Tools for VASP (VTST-Tools).^{38,39} We used the LBFGS optimizer as implemented in VTST-Tools with an energy criteria of 10^{-5} eV and a force criteria of 0.02 eV/Å as well as a reduced plane-wave energy cutoff of 500 eV. We created a 108 atom supercell for FCC Ag, a 144 atom supercell for FCC Ag_3Li and UPb LiAg, a 128 atom supercell for B2 LiAg and BCC Li_3Ag , and a 52 atom supercell for γ_3 - Li_8Ag_5 and γ_1 - $\text{Li}_{11}\text{Ag}_2$. All NEB calculations were performed at constant volume.

Large numbers of symmetrically distinct Li–Ag orderings over the sites of the BCC, FCC, HCP and γ_3 parent crystal structures were generated with the Clusters Approach to Statistical Mechanics (CASM) code.^{40–43} CASM was also used to construct cluster expansion Hamiltonians for the configurational energies of the BCC, FCC, HCP, and γ_3 parent crystals using first-principles training data and to perform Monte Carlo simulations for the purpose of calculating free energies and chemical potentials.⁴⁴ Symmetrically distinct hops and hop environments for NEB calcula-

tions were also enumerated with CASM.^{40,44}

3 Phase stability in the $\text{Li}_x\text{Ag}_{1-x}$ alloy

3.1 Zero kelvin stability

The experimental phase diagram of the $\text{Li}_x\text{Ag}_{1-x}$ alloy has a Ag-rich FCC solid solution that extends to approximately $x = 0.4$, a BCC-based B2 LiAg intermetallic compound, and three lithium-rich intermetallic phases labeled γ_1 , γ_2 , and γ_3 .^{11–14} The three γ phases belong to a family of intermetallic compounds known as γ -brass. The prototypical γ -brass, Cu_5Zn_8 , can be viewed as a superlattice ordering of the sites of the BCC lattice in which one out of every 27 sites contains a structural vacancy. This prototype has been reported in many alloys, including Ag-Zn, Au-Zn, and Fe-Al.^{45,46} The crystal structure of γ_3 - Li_8Ag_5 is well characterized and has the same atomic ordering as Cu_5Zn_8 .^{15,16} However, the crystal structures and Li–Ag orderings of the γ_1 and γ_2 phases are not known, and uncertainties remain about the composition intervals in which these intermetallics are stable.

To further elucidate phase stability in the $\text{Li}_x\text{Ag}_{1-x}$ alloy system, we extend the analysis of Xie et al.¹⁸ and Braga et al.¹⁷ by performing a large number of DFT-PBE calculations of systematically enumerated Li–Ag orderings over different parent crystal structures, including FCC, BCC, HCP, and γ -brass structures. Details of the different structures and chemical orderings considered in this work are described in the Supporting Information.

Figure 1 shows the formation energies as calculated with DFT-PBE of all the structures considered in this study. The formation energies of FCC, BCC, and γ -brass structures are shown in purple, green, and orange, respectively. Formation energies of structures that contain structural vacancies but that are not derived from γ -brass are shown as red triangles. Consistent with past work of Xie et al.¹⁸ and Braga et al.,¹⁷ FCC orderings are stable up to $x = 0.4$ and the B2 LiAg ordering on BCC is the ground state at $x = 0.5$. On the lithium-rich side, many structures derived

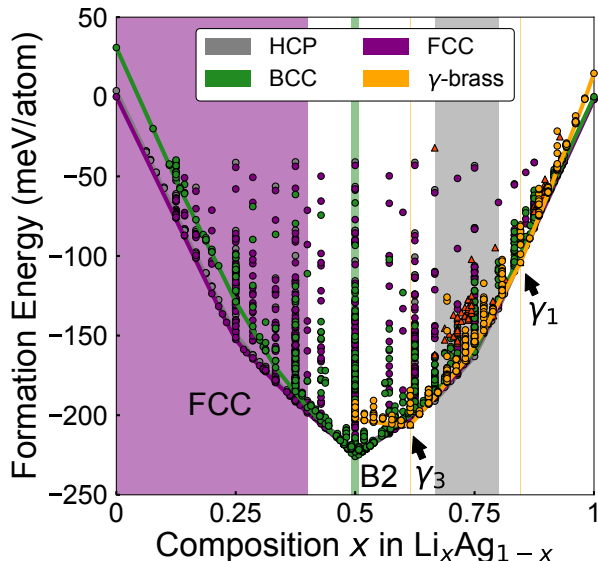


Figure 1: The DFT formation energies of different Li–Ag orderings over the sites of the FCC (purple), BCC (green), HCP (gray), and γ (orange) parent crystal structures. Red triangles denote γ -like structures collected from DFT databases or generated by tiling local γ_1 and γ_3 motifs on a Li-rich BCC parent structure.

from γ -brass by enumerating anti-site defects on the Li and Ag sublattices are close to the convex hull. The γ_3 - Li_8Ag_5 structure at $x = 0.62$ is found to be a global ground state. Another brass-derived structure, with a stoichiometry of $\text{Li}_{11}\text{Ag}_2$, is predicted to be a global ground state at $x = 0.85$. We tentatively refer to this latter ground state as γ_1 - $\text{Li}_{11}\text{Ag}_2$ since its composition coincides with the composition at which γ_1 is reported to exist in the experimental phase diagram.¹¹ This structure was missed in the studies of Xie et al.¹⁸ and Braga et al.,¹⁷ but can be found in the recently published GNoME structure search database.⁴⁷ We independently discovered this structure via enumeration of anti-site defects on γ_3 . None of the γ structures originally proposed by Freeth and Raynor¹² lie on the convex hull.

Surprisingly, HCP-based phases, whose formation energies are shown in gray, are predicted to be ground states in the vicinity of $x = 0.75$. This becomes more evident in Figure 2, which shows the convex hull in the vicinity of $x = 0.75$. While the γ_3 and γ_1 phases are global ground states, there are three Li–Ag configurations on the HCP parent crystal that reside on the convex hull in the

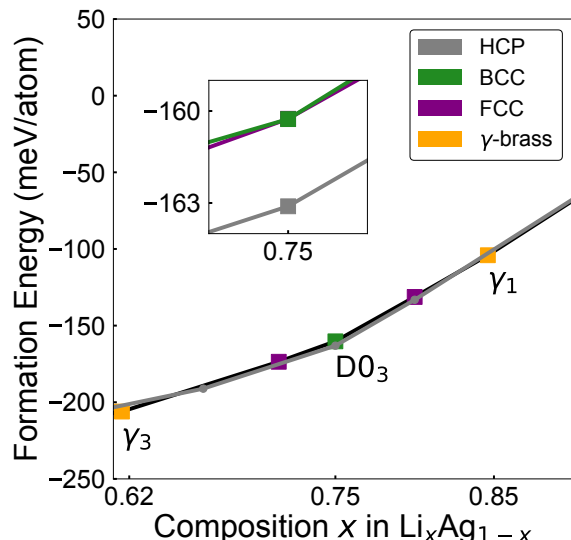


Figure 2: The convex hull and stable phases in the region around $x = 0.75$. At $x = 0.75$, the BCC D0_3 ordering and its strained FCC variant (D0_2) are degenerate in energy as shown in the inset. The HCP variant is roughly 3 meV/atom lower.

vicinity of $x = 0.75$. This composition coincides with that of γ_2 , an intermetallic whose structure has not been characterized. There is no experimental evidence for an HCP based Li_3Ag compound, and we revisit the predicted stability of HCP in the next section.

Figure 1 shows that there are many structures with formation energies close to the convex hull. The B2 LiAg ground state is able to tolerate anti-site defects, as manifested by the large number of configurations having anti-site disorder with formation energies on or very close to the convex hull around $x = 0.5$. It is common for B2 intermetallic compounds to also host high concentrations of vacancies, as in B2 NiAl .^{28,48} However, as detailed in Section 4, DFT calculations performed on large supercells of B2 LiAg containing vacancies predict formation energies that are well above the convex hull.

Figure 3 shows the crystal structures of four compounds that are either ground states or nearly degenerate with ground states. Ag_3Li has the FCC-based D0_{22} structure shown in Figure 3a and is the ground state at $x = 0.25$. Closely related to D0_{22} is LiAg with the UPb ordering shown in Figure 3b. Both orderings share the same super-

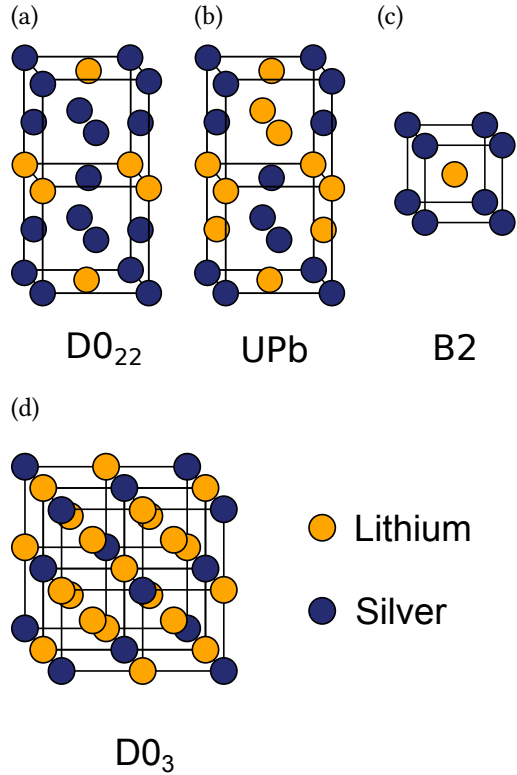


Figure 3: Intermetallic phases in the lithium-silver system calculated with DFT. Orange atoms are lithium and blue are silver. The FCC $D0_{22}$ phase (a) is stable at $x = 0.25$ and the BCC B2 phase (b) is stable at $x = 0.5$. The FCC UPb phase (c) is metastable at $x = 0.5$ with respect to B2 and the BCC $D0_3$ (d) phase is metastable at $x = 0.75$ with respect to HCP.

lattice, differing only in the occupancy of one of the sublattices. The UPb structure can be derived from $D0_{22}$ Ag_3Li by replacing one out three of the Ag by Li. The resulting equiatomic LiAg UPb structure is predicted to be only 0.8 meV/atom higher in energy than the B2 LiAg ground state shown in Figure 3c. The UPb form of LiAg was discovered by Pavlyuk et al.¹⁹ when they studied the evolution of a B2 LiAg sample and found that it spontaneously transformed to the UPb structure in a matter of hours. Also shown in Figure 3d is Li_3Ag in the BCC-based $D0_3$ structure. This structure has a formation energy that is slightly higher than the HCP ground state structure at $x = 0.75$.

The γ_3 and γ_1 ground states are shown in Figure 4. They are very similar to each other in that they are both a particular Li–Ag ordering over the sites of the BCC lattice and have an identical supercell. The supercell is determined by the periodicity of structural vacancies, which are present at a concentration of $1/27$. Figure 4a shows the Li–Ag–vacancy ordering of γ_3 on an ideal BCC lattice, while Figure 4b shows the structure after atoms in the vicinity of the vacancies undergo significant relaxations. A vacancy in the BCC lattice is surrounded by eight nearest neighbor sites that form a cube. In the γ_3 structure, four of the eight sites are occupied by Ag and four are occupied by Li, forming two interpenetrating tetrahedra as shown in Figure 4c. The Li tetrahedron contracts towards the vacancy while the Ag tetrahedron expands, resulting in a highly distorted local environment in the immediate vicinity of the vacancy. The second nearest neighbor shell of the vacancy, which forms an octahedron, is filled by Ag atoms.

The γ_1 structure can be generated from γ_3 by simply replacing the silver in the second nearest neighbor shell of the vacancy by lithium atoms.

In summary, our analysis of zero kelvin phase stability confirms the stability of FCC, B2 and γ_3 . It furthermore leads to the prediction of a stable phase at $x = 0.85$ that is derived from γ_3 and that we refer to as γ_1 . Surprisingly, HCP based phases are stable at compositions in which a γ_2 phase is reported in the experimental literature.^{11–14} To further shed light on phase stability at lithium-rich compositions, we explore energy surfaces of low energy BCC orderings along the Bain and Burgers paths, which connect BCC to FCC and

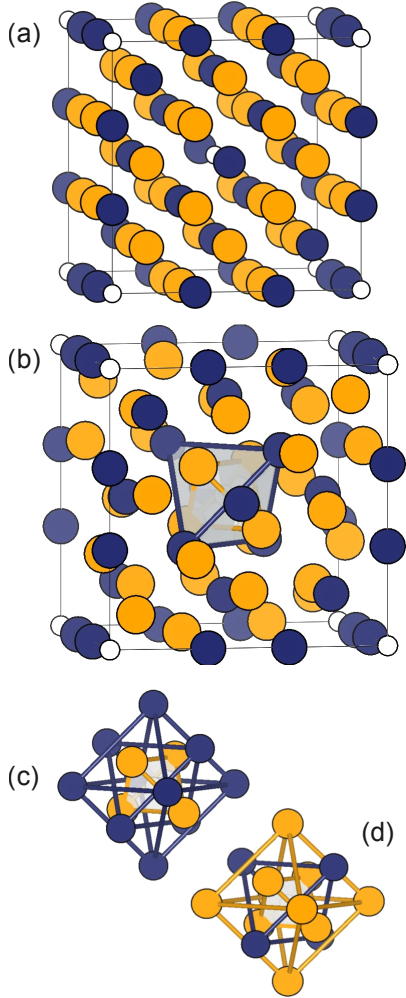


Figure 4: The structure of the lithium-rich γ intermetallic phases. Orange atoms are lithium, blue are silver, and white are structural vacancies. Part (a) shows the γ_3 - Li_8Ag_5 ordering projected onto an ideal BCC crystal. Part (b) shows the relaxed γ_3 structure with the tetrahedron of silver around the structural vacancy highlighted. Parts (c) and (d) show the tetrahedral and octahedral shells of γ_3 and γ_1 - $\text{Li}_{11}\text{Ag}_2$, respectively.

HCP, respectively. This is motivated by past predictions of very flat energy surfaces for pure Li along the Bain and Burgers paths.³¹

3.2 Energy along structural transformation paths

The zero kelvin energy surface of lithium metal is highly unusual. The energies of lithium in the BCC structure and in close-packed structures, such as FCC, HCP, DHCP, and 9R, are essentially degenerate, differing by less than 1–2 meV/atom from each other.³⁰ Furthermore, the barriers along pathways that connect BCC to any of the close-packed phases are almost nonexistent and do not exceed more than 1–2 meV/atom.³¹ These energy differences are within the numerical accuracy of DFT total energy calculations. The very flat energy landscape of lithium implies that anharmonic vibrational excitations are essential in stabilizing the room temperature BCC phase. Furthermore, it likely has fundamental implications about elastic and plastic deformation mechanisms of lithium.

Two important pathways that connect BCC to close-packed structures are the Bain path, which transforms BCC into FCC by a tetragonal elongation, and the Burgers path, which transforms BCC into HCP by combining a tetragonal compression with an atomic shuffle. The Bain and Burgers paths can be described with the same symmetry-adapted tetragonal strain order parameter defined according to $e_3 = 1/\sqrt{6}(2E_{zz} - E_{xx} - E_{yy})$.^{31,49} The Cartesian strains in this definition measure deformations relative to a BCC structure with its cubic unit cell vectors aligned along the Cartesian axes. A positive e_3 takes BCC to FCC, while a negative e_3 coupled with an internal shuffle converts BCC to HCP.^{31,49} The dark yellow curve in Figure 5a labeled Li is the energy of lithium metal as a function of e_3 (without accounting for the shuffle of the Burgers path) and clearly reveals the unusual flatness of the lithium energy surface.

Figure 5a shows that the addition of Ag to Li modifies the energy surface slightly along the Bain path, but it is only at the equiatomic composition in the B2 ordering that BCC becomes a clear and robust minimum as a function of e_3 . For the silver-rich phases in Figure 5b, the FCC struc-

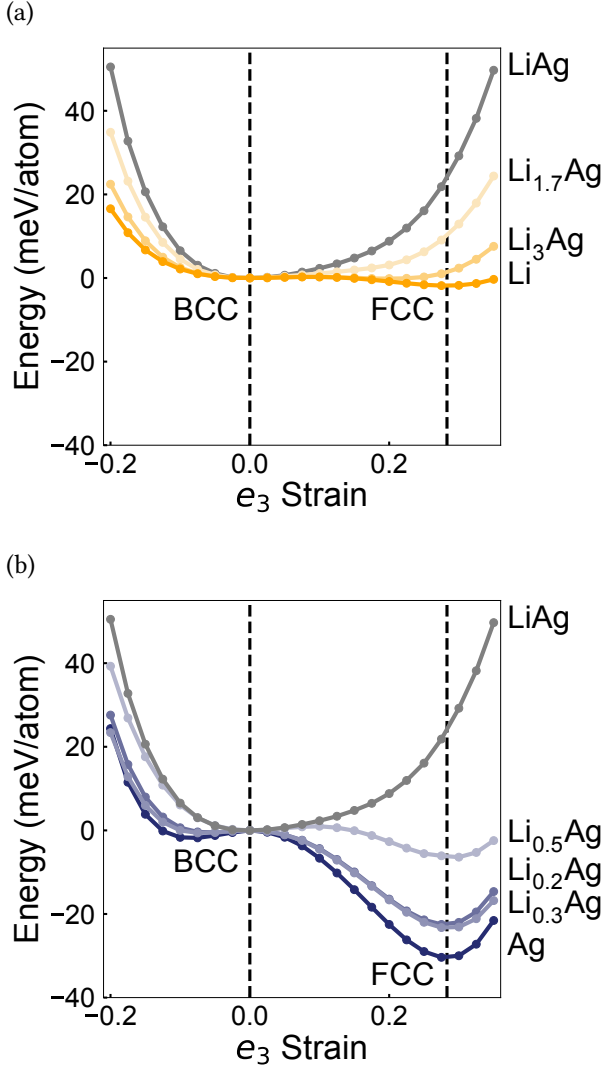


Figure 5: Energy surfaces for lithium-rich (a) and silver-rich (b) phases with respect to BCC upon application of tetragonal e_3 strain in the absence of atomic shuffles. The lithium-rich energy surfaces are quite flat along the Bain path, while the silver-rich energy surfaces show an increasing preference for FCC as the silver concentration is increased. The B2 LiAg ordering (gray) is only stable for $e_3 = 0$.

ture is stabilized at positive e_3 strain, and the minimum becomes deeper relative to BCC as the concentration of Ag increases, with the deepest well occurring for pure Ag. This is consistent with the predictions of the previous section, which showed that FCC $\text{Li}_x\text{Ag}_{1-x}$ is the stable phase for $x \leq 0.4$.

The main uncertainties in the Li–Ag phase diagram are at lithium-rich concentrations. Our analysis of zero kelvin phase stability (Section 3.1) led to the surprising prediction that orderings of Li and Ag over the sites of the HCP parent crystal structure are stable around $x = 0.75$. Figure 6a shows the energy of the BCC-based D0_3 Li_3Ag compound along both the Bain and the Burgers paths. Straining D0_3 along the Bain path generates the D0_{22} structure of Li_3Ag , an ordering on the the FCC lattice, while deforming it along the Burgers path generates an HCP structure with the ordering shown in Figure 6b. The energies of D0_3 and D0_{22} are essentially equal, while the energy of the HCP phase that forms upon application of the Burgers path to D0_3 Li_3Ag is 2.8 meV/atom lower than that of D0_3 .

Although an ordering on HCP of Li_3Ag is predicted to be a global ground state at zero kelvin, it is clear in Figure 6 that its energy is only slightly below that of D0_3 Li_3Ag and that the energy along the Burgers and Bain paths is very flat as is seen in pure lithium. Taken together, the energy surfaces of Figures 5 and 6 reveal an unusual ambivalence for BCC, FCC, and HCP, with negligible barriers along the Bain and Burgers paths in lithium-rich $\text{Li}_x\text{Ag}_{1-x}$ alloys. This raises fundamental questions about the true nature of the room temperature phase of lithium rich $\text{Li}_x\text{Ag}_{1-x}$. Vibrational excitations tend to favor BCC over close-packed structures at elevated temperature due to the more open crystal structure of BCC. Hence, similar to lithium, anharmonic vibrations will likely play an essential role in stabilizing the room temperature phase.

The energy surfaces along the Bain and Burgers paths are also highly unusual at the stoichiometric LiAg composition. The B2 form of LiAg favors the BCC structure and has no local minima at non-zero e_3 strains along the Bain and Burgers paths as shown by the green line in Figure 7. However, as pointed out in the previous section, there is a second, metastable ordering at the same compo-

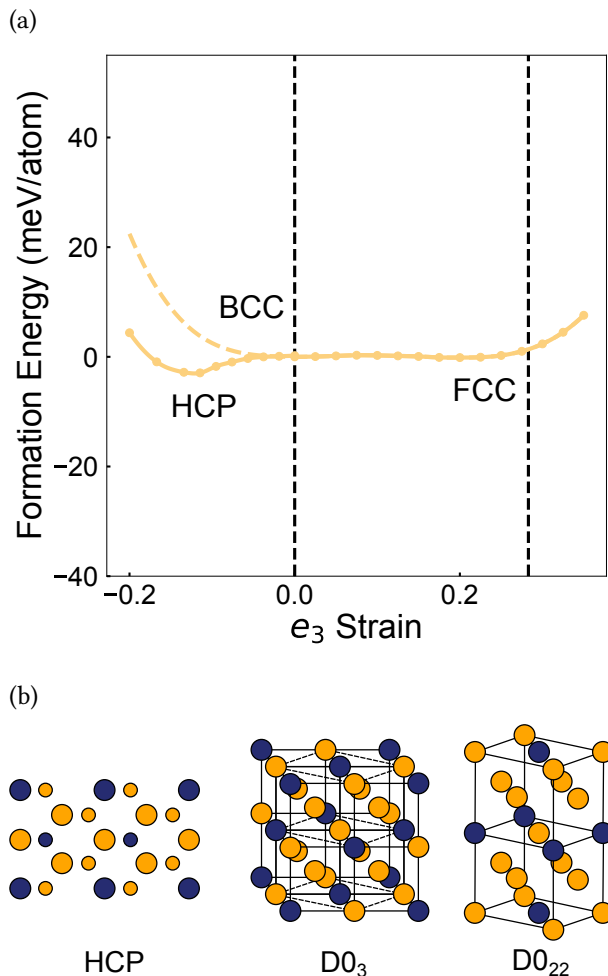


Figure 6: Strain surface at $x = 0.75$ for the $D0_3$ ordering. Applying a positive e_3 strain along the Bain path results in the FCC $D0_{22}$ structure, while applying a negative strain and shuffle along the Burgers path results in an HCP structure. The dotted line represents a purely strain-based deformation along negative e_3 with no atomic shuffle.

sition that favors the FCC UPb structure and that has also been observed experimentally.¹⁹ The energy of this ordering as a function of e_3 is shown by the purple line in Figure 7. This ordering, when transformed to BCC along the Bain path, adopts the Zintl B32 ordering on BCC, which is also seen in LiAl, LiGa, and LiZn.³²

The B32 Zintl form of LiAg at $e_3 = 0$ is unstable in the BCC structure, but exhibits local minima for non-zero e_3 coinciding with FCC and HCP. The HCP to B32 transition was previously identified by Kolli et al.⁵⁰ The FCC state, having the UPb ordering, is only 0.8 meV/atom above that of B2 LiAg. Hence, the two phases are almost degenerate in energy: one in the BCC phase, the other in the FCC phase.

3.3 Voltage curves

We next investigate phase stability at finite temperature and in particular focus on room temperature electrochemical properties. Free energies at elevated temperatures have a sizable contribution from the entropy that arises from thermal excitations at the atomic scale. An important source of entropy in alloys arises from configurational degrees of freedom due to the many possible ways of arranging atoms over the sites of different parent crystal structures. These can be accounted for by using cluster expansion surrogate models^{41,51,52} to describe the dependence of the energy on chemical ordering, thereby enabling a rigorous calculation of configurational entropy using Monte Carlo simulations.⁵³

Cluster expansions were constructed for the FCC and BCC parent crystal structures by fitting interaction coefficients to the large dataset of formation energies shown in Figure 1. A cluster expansion was also constructed for a parent crystal structure based on the γ_3 phase by allowing for Li occupancy on the Ag sublattice of γ_3 . The cluster expansions were used in Monte Carlo simulations to calculate thermodynamic properties, including free energies and chemical potentials. Based on experimental studies of the Li–Ag system, we did not consider HCP structures and we suppressed the FCC phase above $x = 0.5$.

Figure 8 shows the calculated voltage curve at room temperature (300 K) derived from the free

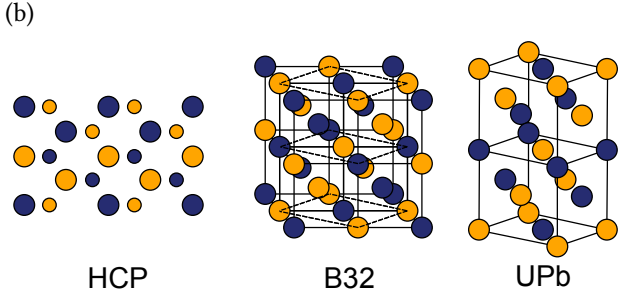
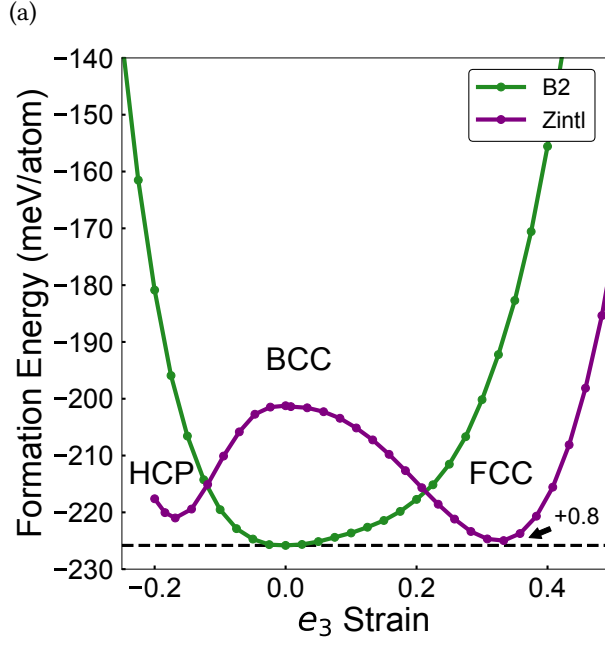


Figure 7: Strain surfaces at $x = 0.5$ for the B2 and B32 orderings. Applying a positive e_3 strain to the B32 ordering along the Bain path results in the FCC UPb structure, while applying a negative strain and atomic shuffle along the Burgers path results in an HCP structure. FCC UPb is 0.8 meV/atom higher in energy than B2.

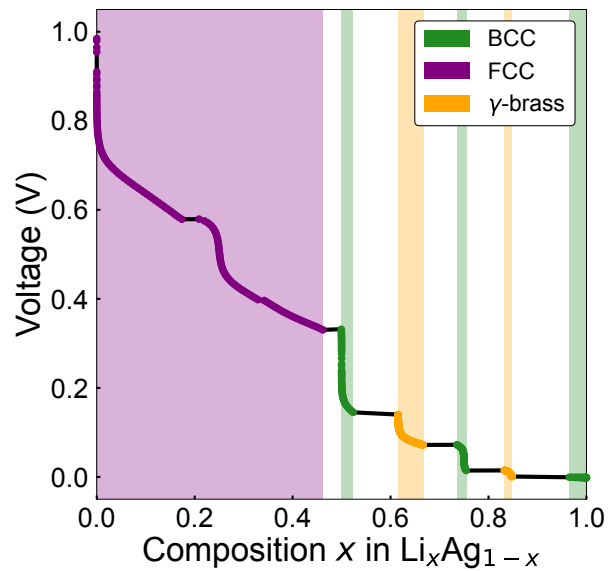


Figure 8: Calculated equilibrium voltage curve at 300 K considering the BCC, FCC, and γ parent crystal structures. The voltage curve shows an FCC solid solution up to $x = 0.46$ with some ordering around $x = 0.25$ followed by strongly ordered intermetallic phases corresponding to B2, γ_3 , $D0_3$ Li_3Ag , and γ_1 .

energies of the FCC, BCC, and γ_3 parent crystal structures. A sloping voltage profile signifies a disordered solid solution, while an abrupt step occurs at compositions at which an ordered compound is stable. Plateaus in a voltage profile correspond to two-phase regions where the chemical potentials are constant.⁵³ The FCC phase is stable below $x = 0.46$ as shown by the purple region in Figure 8. With the exception of a small step at $x = 0.25$, which arises from the stability of the $D0_{22}$ $LiAg_3$ ordered phase shown in Figure 3a, the FCC phase forms a solid solution. The sharp step at $x = 0.5$, shown in green, is due to the B2 $LiAg$ compound, which tolerates a limited degree of off-stoichiometry due to anti-site defects. Above $x = 0.6$, the γ_3 phase becomes stable and is capable of accommodating an excess of lithium through the substitution of Ag atoms by Li in the stoichiometric Li_8Ag_5 compound. The step at $x = 0.75$, shown in orange, is due to the $D0_3$ Li_3Ag compound, which is separated by two plateaus from γ_3 and γ_1 . The γ_1 phase appears as the small orange step at $x = 11/13$.

In calculating the room-temperature voltage curve, we have neglected contributions to the free

energy from vibrational excitations. The very flat energy surfaces along the Bain and Burgers paths of low energy orderings in the $\text{Li}_x\text{Ag}_{1-x}$ alloy at lithium rich compositions indicate that vibrational excitations play a crucial role in stabilizing the room temperature phases observed experimentally. Unfortunately, the high degree of anharmonicity at lithium rich concentrations precludes the use of phonon theories such as the quasi-harmonic approximation to calculate the vibrational free energy. Instead, statistical mechanics approaches that explicitly account for anharmonicity will be necessary to determine the room temperature crystal structure of Li-rich $\text{Li}_x\text{Ag}_{1-x}$ alloys and their thermodynamic properties.^{42,54–62} This is beyond the scope of this study, but including anharmonic vibrational excitations may resolve the ambiguity around $x = 0.75$ and the unexpected stability of the HCP phases at zero kelvin by stabilizing the BCC form of Li_3Ag at elevated temperatures in a manner similar to the stabilization of BCC Li.

4 Diffusion in $\text{Li}_x\text{Ag}_{1-x}$

Substitutional diffusion in FCC and BCC alloys is generally mediated by vacancies.^{20,21,23,27,29} It therefore depends not only on the migration barriers of individual hops, but also on the equilibrium vacancy concentration. The migration barrier and equilibrium vacancy concentration tends to depend on the alloy concentration and can be sensitive to varying degrees of short- and long-range order among the constituents.^{22,23,27,28,63}

In most substitutional alloys, vacancies are entropically stabilized, having a positive formation energy. There is some ambiguity as to defining a vacancy formation energy in an alloy since the site that is made vacant can be occupied by any of the constituents of the alloy.²² A vacancy formation energy within the grand canonical ensemble can be defined according to

$$\Delta\Omega = E(N_{\text{Va}} = 1) - E(N_{\text{Va}} = 0) - \Delta N_{\text{Li}}\mu_{\text{Li}} - \Delta N_{\text{Ag}}\mu_{\text{Ag}} \quad (1)$$

where $E(N_{\text{Va}} = 1)$ is the energy of a large super cell containing a vacancy in an ordered or disor-

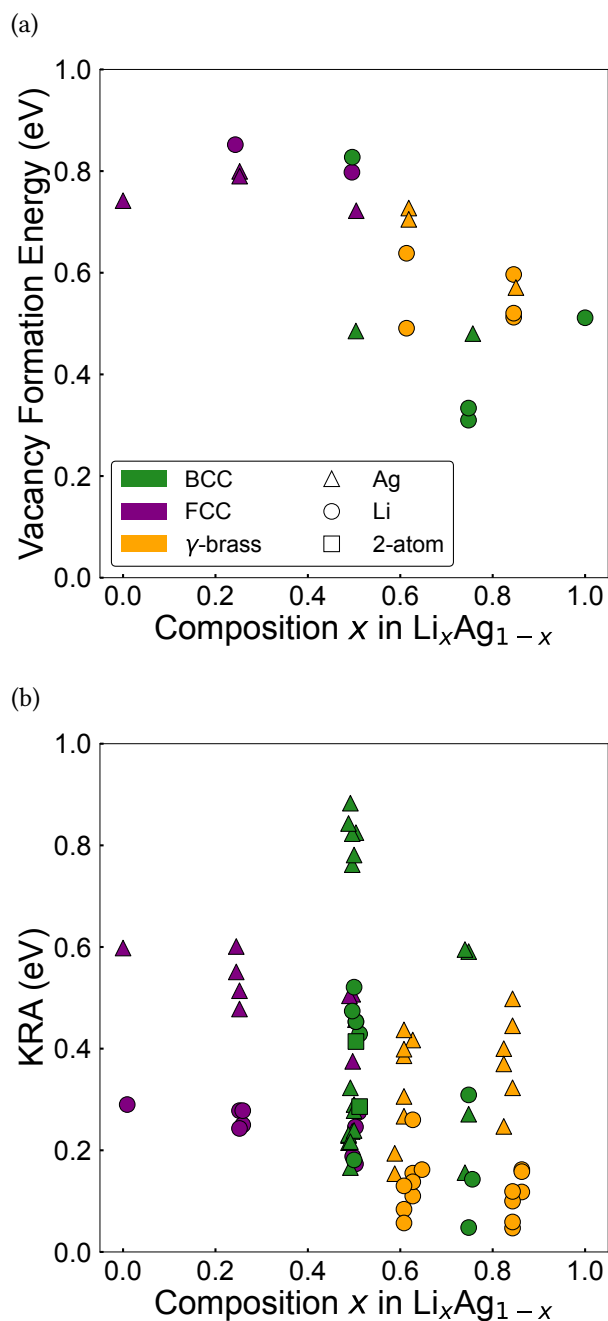


Figure 9: Part (a) shows vacancy formation energy at 300 K for single vacancies in BCC, FCC, and γ phases. Part (b) shows all calculated KRA barriers vs. composition. Points are colored by parent crystal structure. Shapes in (a) represent the type of vacancy, while shapes in (b) represent the atom which is hopping.

der configuration and $E(N_{\text{Va}} = 0)$ is the energy of the same super cell without a vacancy. The ΔN_{Li} and ΔN_{Ag} are the changes in the number of Li and Ag atoms upon introducing a vacancy into the supercell while μ_{Li} and μ_{Ag} are the chemical potentials of the Li and Ag within the alloy. The chemical potentials can be extracted from the free energy of the alloy as for example calculated with Monte Carlo simulations (Section 3.3).

Figure 9a shows formation energies as calculated according to Eq. 1 for different concentrations x in $\text{Li}_x\text{Ag}_{1-x}$ in the FCC, BCC and γ phases. The vacancy formation energies are predicted to be especially large in the silver rich FCC phase, having values in the range of 0.8 eV. In pure Ag, for example, the vacancy formation energy is predicted to be $\Delta\Omega = 0.74$ eV. This value leads to an equilibrium vacancy concentration of $x_{\text{Va}} \approx 10^{-13}$ at a temperature of $T = 300$ kelvin, as estimated using $x_{\text{Va}} = e^{-\Delta\Omega/k_B T}$ (k_B is the Boltzmann constant).⁶⁴ While contributions to the vacancy formation free energy from vibrational excitations have been neglected in this estimate, these are not expected to modify the exceptionally low vacancy concentration by more than an order of magnitude.⁶⁵

Of particular note in Figure 9a is the large difference in vacancy formation energies between FCC-based and BCC-based structures. Furthermore, for the well-ordered intermetallic phases, the vacancy formation energy depends strongly on the sublattice on which it is introduced. For example, the cost of introducing a vacancy on the Ag sublattice in B2 LiAg is substantially smaller than that of introducing a vacancy on the Li sublattice. The lowest vacancy formation energies occur in the BCC based D0_3 Li_3Ag compound at $x = 0.75$, where the formation energy to create a vacancy on the Li sublattice is slightly larger than 0.3 eV.

Figure 9b collects kinetically resolved activation (KRA) barriers in the FCC, BCC and γ structures for different alloy compositions and Li–Ag orderings. The KRA for a hop^{41,66} is calculated as the peak energy along the migration path minus the average of the end state energies and is thereby independent of the direction of a hop. Figure 9b shows that the migration barriers tend to decrease with increasing Li concentration, with the γ_3 , D0_3 Li_3Ag and γ_1 compounds having hops

with very low migration barriers. The steady reduction in the migration barriers and in the vacancy formation energies with increasing Li concentration indicates that Li-rich alloys will have higher diffusion coefficients than Ag-rich alloys. The hop mechanisms in the various intermetallic compounds of the Li–Ag binary are complex and are described in more detail in the following sections.

4.1 Elementary migration barriers in FCC $\text{Li}_x\text{Ag}_{1-x}$

The energy barriers for nearest neighbor silver and lithium hops are relatively low in FCC silver. Figure 10 shows the energy as a Li or a Ag atom migrates into a neighboring vacancy as calculated with DFT-PBE using the NEB method. The migration barrier of a dilute Li solute into a vacancy within its nearest neighbor shell in an otherwise pure Ag supercell is predicted to be approximately 0.25 eV. The migration barrier for a Ag hop in pure Ag, in contrast, is predicted to be twice as large with a value of approximately 0.5 eV. These barriers are low when compared to other FCC alloys such as $\text{Al}_{1-x}\text{Li}_x$ and $\text{Ni}_{1-x}\text{Al}_x$.^{23,29} The barriers for second nearest neighbor hops are significantly higher, ranging between 1.5 eV and 2.5 eV and indicate that second nearest neighbor hops in FCC Ag are negligible.

While the tracer diffusion coefficients of the constituents of a concentrated alloy must be calculated with numerical approaches such as kinetic Monte Carlo,^{21,23,29,67–69} it is possible to calculate diffusion coefficients analytically in the dilute limit.²⁰ The tracer diffusion coefficient of Li in FCC Ag, for example, can be calculated with

$$D^* = x_{\text{Va}} g r^2 f \nu^* e^{-\Delta E_B/k_B T} \quad (2)$$

where g is a geometric factor that is equal to 2 for FCC, $f = 0.78$ is the correlation factor for FCC,⁷⁰ x_{Va} is the equilibrium vacancy concentration (which we estimate is on the order of 10^{-13}), $r = 2.93 \times 10^{-8}$ cm is the hop distance, ΔE_B is the migration barrier, k_B is the Boltzmann constant, and T is the temperature. At room temperature, this expression predicts a Li tracer diffusion coefficient of 10^{-20} cm^2/s when using the

calculated Li migration barrier and vacancy formation energy in FCC Ag and an upper bound for the vibrational prefactor, $\nu^* = 10^{13}$ Hz. This is an exceedingly low diffusion coefficient and indicates that the formation of an FCC $\text{Li}_x\text{Ag}_{1-x}$ solid solution through interdiffusion when pure Ag is electrochemically alloyed with Li will occur very slowly at room temperature.

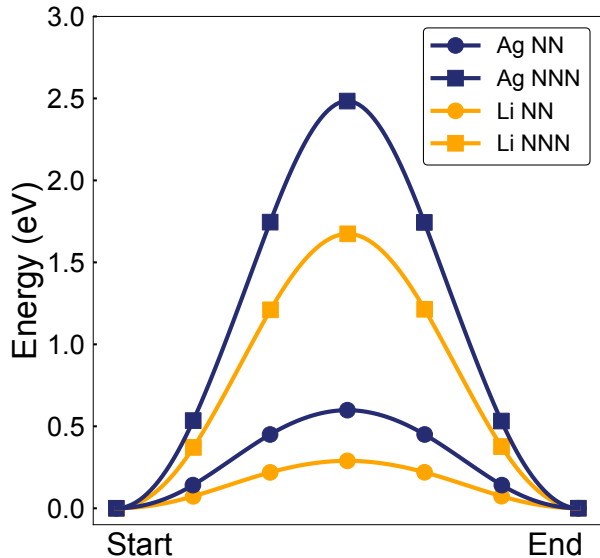


Figure 10: KRA barriers for nearest and second nearest neighbor hops in FCC Ag. Ag hop barriers are larger than corresponding Li hop barriers, and second nearest neighbor barriers are much larger than nearest neighbor barriers.

4.2 Diffusion mechanisms in B2 $\text{Li}_x\text{Ag}_{1-x}$

The B2 structure of LiAg is a superlattice ordering on the BCC parent crystal structure.⁷¹ The cubic unit cell consists of a cubic Li sublattice and a cubic Ag sublattice. In perfectly ordered B2 LiAg, each Li site is surrounded by eight Ag atoms, and vice versa. When a Li or Ag atom performs a nearest neighbor hop, it migrates from one sublattice to the other sublattice, and in the process increases the number of point defects.²⁸ A Ag atom of B2 LiAg that performs a nearest neighbor hop into a vacancy on the Li sublattice, for example, goes from an initial state consisting of one vacancy on the Li sublattice to a final state containing a Ag anti-site defect on the Li sublattice and

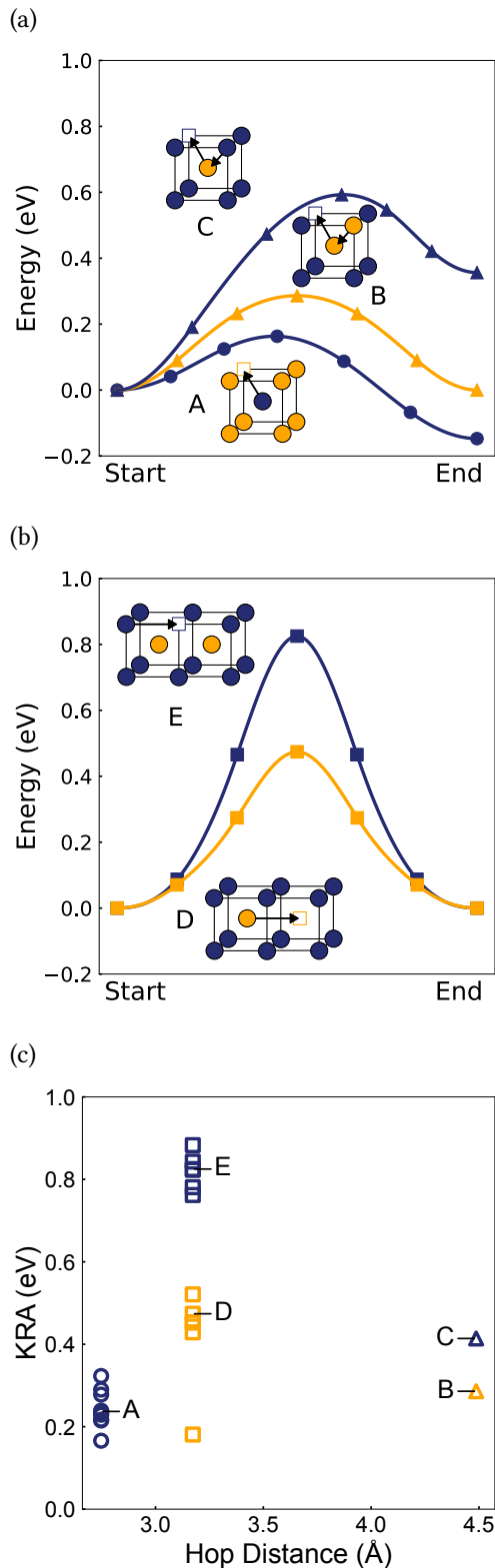


Figure 11: NEB paths for nearest neighbor (a) and second nearest neighbor (b) hops in B2 LiAg. Nearest neighbor Ag hops are stable (A), while nearest neighbor Li hops require a 2-atom hop mechanism (B, C). Part (c) shows KRA barriers vs. vacancy displacement distance. Prototype hops without additional defects are labeled.

a vacancy on the Ag sublattice. Hence, diffusion in B2 that relies on nearest neighbor hops necessarily results in an increase in the degree of disorder, thereby disrupting thermodynamically favored long-range order.

The B2 LiAg compound exhibits unique hop mechanisms and barriers. For example, our DFT calculations predict that a nearest neighbor Li hop into a vacancy on the Ag sublattice is unstable. A Li atom that is moved from the Li sublattice to a nearest neighbor Ag vacancy is predicted to spontaneously relax back to its initial state on the Li sublattice. In contrast, a Ag nearest neighbor hop is not only possible, but leads to a lowering of the energy of the crystal, as is evident in Figure 11a, where the end state of the Ag nearest neighbor hop is lower than that of the initial state. This indicates that a Ag anti-site defect next to a vacancy on the Ag sublattice is energetically preferred over a lone vacancy on the Li sublattice.

While a nearest neighbor Li hop from the Li sublattice to the Ag sublattice is predicted to be unstable, a Li can still migrate to the Ag sublattice if a second atom follows in its wake to fill the vacancy left by the first Li, as illustrated in Figure 11a. The energy barrier for this 2-atom hop is lower if the second atom is also Li (Figure 11a). The end states then have the same energy since the total number of Li anti-site defects is preserved. The Li and Ag of B2 LiAg are also able to perform second nearest neighbor hops. Second nearest neighbor hops in the B2 structure keep the migrating atom on the same sublattice and therefore preserve long-range order. The energy barriers for second nearest neighbor lithium and silver hops without anti-site defects (Figure 11b) are about a third of the size of those in FCC silver (Figure 10). This is because the BCC crystal structure is more open than the close-packed FCC crystal structure.

The barriers for Li and Ag hops in B2 LiAg shown in Figure 11a and 11b are calculated with the minimum number of defects. However, the B2 form of LiAg can tolerate anti-site defects, which can affect migration barriers due to local changes in the degree of ordering among Li and Ag.

Figure 11c shows KRA barriers for 22 different states containing anti-site and vacancy point defects in the background B2 ordering. Different degrees of anti-site disorder around a migrating Li

or Ag does affect migration barriers, as is evident by the spread in KRA values for each hop type, but the spread is narrow. Figure 11c indicates that nearest neighbor Ag hops have the lowest barrier of approximately 0.25 eV, while Li second nearest neighbor hops and two-atom hops have KRA barriers that are slightly higher, averaging around 0.4 eV and 0.3 eV, respectively. The KRA barriers suggest that both Li and Ag should be mobile at room temperature, provided that there is a sufficient number of vacancies to mediate diffusion.

4.3 Migration barriers in γ_3 and γ_1

The γ_3 crystal structure is significantly more complex than the FCC and BCC intermetallic compounds, consisting of many symmetrically distinct hop types. As described in Section 3.1, the γ_3 phase can be viewed as a particular Li–Ag ordering over the sites of a BCC parent lattice that contains a periodic array of structural vacancies. In contrast to B2 LiAg, each Li site of the γ_3 Li₈Ag₅ phase is connected to other Li sites by nearest neighbor hops. Figure 12a shows each symmetrically distinct hop in γ_3 . For ease of viewing, the γ_3 ordering has been projected onto an ideal BCC crystal lattice. Due to structural relaxations as a result of the Li–Ag ordering and the presence of structural vacancies, there is some variability in the length of each symmetrically distinct hop. Figure 12b collects the KRA barriers for each symmetrically distinct hop in γ_3 . The hops with shorter lengths, labeled A, B, C, D, F, H, and J correspond to nearest neighbor hops in the ideal BCC lattice, while E, G, and I are second nearest neighbor hops. The migration barriers for nearest neighbor Li are very low, ranging between 0.1 and 0.2 eV. The Ag migration barriers are slightly higher, but do not exceed 0.45 eV. As in B2, lithium nearest neighbor hops onto the silver sublattice can also be performed as a 2-atom hop.

Because the structural vacancy of γ_3 is very stable, any hop into it originating from its nearest neighbor shell (A, J) is predicted to be unstable. Second nearest neighbor hops originating from the octahedron of sites coordinating the structural vacancy, however, are possible. The second nearest neighbor shell of the structural vacancy in γ_3 is exclusively filled by Ag. The migration barrier for

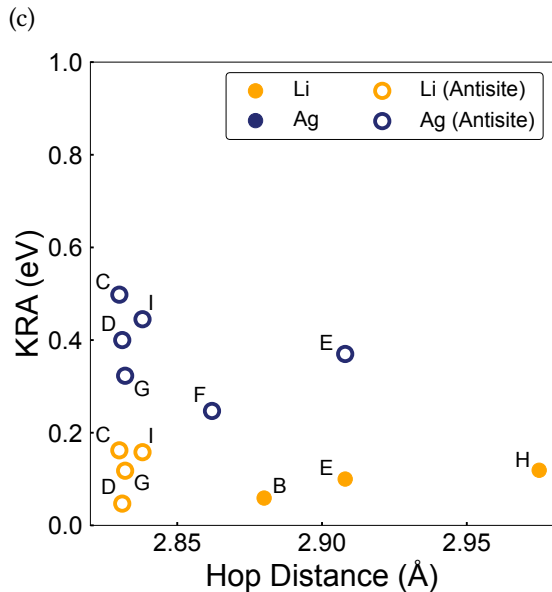
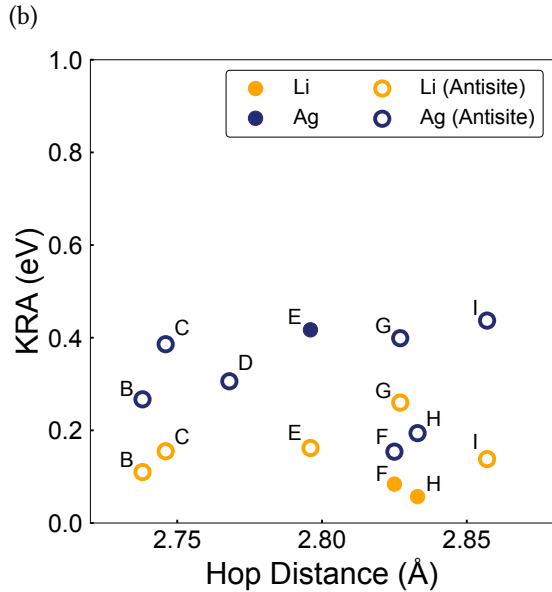
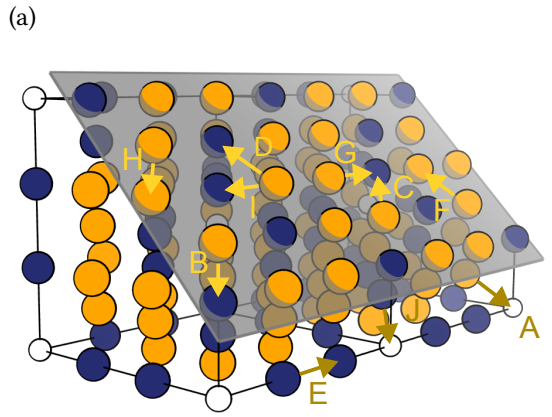


Figure 12: KRA barriers for γ_3 (b) and γ_1 (c). The hop sites are labeled in (a). Orange (blue) circles indicate that a Li (Ag) atom is making the hop. Open circles that the hop requires an anti-site defect.

a Ag hop into the structural vacancy by means of a second nearest neighbor hop is 1.01 eV, and the migration barrier of an anti-site Li atom into the structural vacancy is 0.74 eV. These high barriers for hops into the structural vacancy suggest that the structural vacancy is not very mobile and will remain in place, with Li and Ag diffusing through the crystal by exchanging with thermally induced excess vacancies on the Li and Ag sublattices.

Similar migration barriers are predicted for Li and Ag hops in the related γ_1 phases. These are summarized in Figure 12c

4.4 Migration barriers in $D0_3$ Li_3Ag

Similar to B2 LiAg, the $D0_3$ Li_3Ag crystal structure is a superlattice ordering of Li and Ag over the sites of the BCC lattice. Each Li site in $D0_3$ is connected to other Li sites by nearest neighbor hops. The Ag atoms, in contrast, are isolated and are surrounded by eight Li in their nearest neighbor shell. Li hops can therefore occur without altering long-range order, while Ag nearest neighbor hops necessarily introduce anti-site defects. Figure 13 shows KRA barriers for Li and Ag in $D0_3$ Li_3Ag . The KRA for a Li nearest neighbor hop which preserves the $D0_3$ ordering (A) is remarkably small, with a value of under 0.05 eV. A similar low barrier was predicted for Li nearest neighbor hops in Li_3Sb , which is also stable in the $D0_3$ structure.⁷² Our DFT calculations predict that a Li nearest neighbor hop into a vacancy on the Ag sublattice is unstable, but that a Ag can perform a nearest neighbor hop onto the Li sublattice (hop B) with a barrier of 0.27 eV. As in B2 LiAg, Li can only perform a nearest neighbor hop onto the Ag sublattice through a two-atom hop mechanism. The energy barrier for a 2-atom hop involving two Li atoms is 0.15 eV.

5 Discussion

Lee et al.⁹ demonstrated that a Ag-C composite inter layer, placed between the current collector and solid electrolyte of an all-solid-state battery, plays a beneficial role in controlling the morphology of lithium metal. This has spurred followup studies to determine how Ag interacts

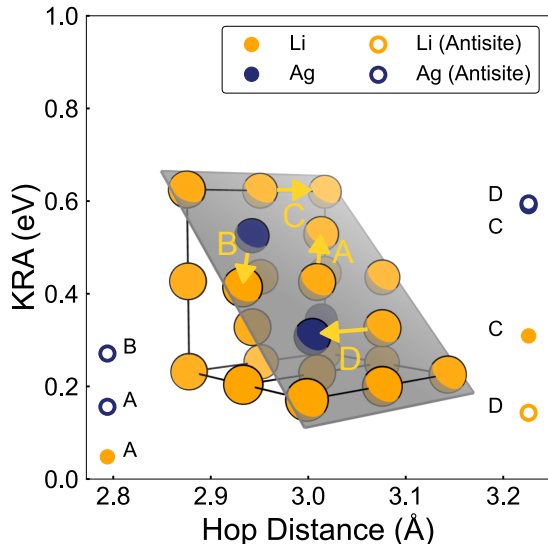


Figure 13: Nearest and second nearest neighbor hops in $D0_3$ Li_3Ag . Orange (blue) circles indicate that a Li (Ag) atom is making the hop. Type B hops are unstable when Li attempts a hop into a vacant Ag site, but it can be realized with a 2-atom hop. Inset shows the Li_3Ag (011) plane.

with Li as Li plates and strips at the anode.¹⁰ The thermodynamic and kinetic properties of the Li–Ag alloy system must be established before a mechanistic understanding of the role of Ag on lithium plating can be developed. The Li-rich portion of the Li–Ag binary phase diagram remains poorly characterized, with reports of the existence of several γ -brass-like intermetallic compounds whose crystal structures and stoichiometries remain unknown.^{11–13} Furthermore, almost nothing is known about the mechanisms of lithium and silver diffusion within the various phases of the Li–Ag system. Our first-principles study of the Li–Ag alloy system builds on the previous work of Bragga et al.¹⁷ and Xie et al.¹⁸ and provides new insights about phase stability and diffusion mechanisms.

New findings in this work include the prediction of an intermetallic ground state having a stoichiometry of $\text{Li}_{11}\text{Ag}_2$, similar to that of the experimentally reported γ_1 phase, and an HCP ground state with a stoichiometry of Li_3Ag . The structure of the $\text{Li}_{11}\text{Ag}_2$ ground state can be derived from the γ_3 brass structure by simply replacing the octahedron of Ag surrounding the structural vacancy of γ_3 by lithium. The prediction of HCP

based Li–Ag orderings on the global convex hull is surprising since there is no experimental evidence for the existence of HCP phases in the Li–Ag binary system. The predicted ground state structures of this work can serve as models to fit and refine diffraction patterns obtained for different lithium-rich compositions such as those gathered via in-situ diffraction during electrochemical lithiation of silver by Jin et al.⁷³

Our study has shown that the uncharacteristically flat energy surface of pure Li along the Bain and Burgers paths³¹ persists upon the addition of Ag to Li. This has relevance in clarifying the absence of any experimental evidence for the HCP crystal structure in the Li–Ag binary system at room temperature, in spite of the fact that the predicted Li_3Ag ground state is an ordering on HCP. We have shown that the HCP Li_3Ag ground state is connected to $D0_3$ Li_3Ag (an ordering on BCC) through the Burgers path. The HCP ground state is only marginally more stable than its $D0_3$ counterpart on the BCC parent crystal, with the energy of the $D0_3$ ordering when deformed along the Burgers and Bain paths being almost as flat as that of pure Li. The extreme form of anharmonicity, as manifested by this high degree of degeneracy of Li-rich $\text{Li}_x\text{Ag}_{1-x}$ alloys, indicates that phonon theories are not applicable and statistical mechanics treatments of vibrational excitations must go beyond the (quasi) harmonic approximation. This will require new statistical mechanics methods that explicitly treat anharmonicity^{42,54–62} or a reliance on Monte Carlo simulations using highly accurate machine learned interatomic potentials that have been explicitly trained to the flat energy landscapes along paths connecting BCC to different close-packed phases.³¹ As in pure Li, which also has a high degree of degeneracy between BCC and close-packed structures,^{30,31} we expect that at $x \approx 0.75$ the BCC crystal will be stabilized at elevated temperature. This more open crystal structure tends to be entropically favored over close-packed crystal structures such as HCP and FCC.

Our calculations have also revealed a high degree of degeneracy between FCC and BCC when Li and Ag are present at equiatomic compositions. The energy surfaces along the Bain and Burgers paths of LiAg (Figure 7a) show that the

favored crystal structure at this composition depends strongly on the ordering of Li and Ag. The B2 ordering of LiAg on the BCC parent structure is very stable. Furthermore, the FCC $L1_0$ counterpart, accessible to B2 along the Bain path, and the HCP B19 counterpart, accessible to B2 along the Burgers path, are unstable and spontaneously relax back to B2. In contrast, the B32 ordering of LiAg on the BCC parent structure is unstable and will spontaneously relax to the FCC UPb structure along the Bain path or an HCP ordering along the Burgers path. The BCC based B2 LiAg and the FCC based UPb structure of LiAg have energies that differ by less than 1 meV. This degeneracy at $x = 0.5$ and the strong dependence of the qualitative shape of the energy surface along the Bain and Burgers paths on ordering at $x = 0.5$ has important implications for phase stability and likely plays a role in determining the kinetics of the experimentally observed phase transformation from B2 LiAg to the UPb form of LiAg during aging.¹⁹

The rate with which Li reacts with Ag to form Li_xAg_{1-x} solid solutions and ordered intermetallic phases depends on the diffusion coefficients of Li and Ag as a function of concentration. Diffusion in substitutional alloys is mediated by vacancies, and therefore depends directly on the equilibrium vacancy concentration.²⁰⁻²³ The vacancy formation energies in FCC Li_xAg_{1-x} are very high (≈ 0.8 eV), which translates into very low vacancy concentrations at room temperature. This coupled with the moderate migration barriers for Li and Ag diffusion in FCC Li_xAg_{1-x} (0.3 eV for Li and 0.6 eV for Ag) results in low diffusion coefficients. That for Li in the dilute limit is predicted to be of the order of 10^{-20} cm²/s. Hence, diffusion in the FCC Li_xAg_{1-x} solid solution at room temperature will be very sluggish. Only with nanoparticles of Ag, where the diffusion distances are very short, will an electrochemical signature of the FCC Li_xAg_{1-x} solid solution at high voltage (between 0.7 and 0.3 V) be evident in experimental voltage profiles. When FCC Ag is present as larger particles, Li will not readily dissolve to form an FCC Li_xAg_{1-x} solid solution during electrochemical deposition. Instead, a B2 shell will rapidly form on the surface of FCC Ag particles.⁷⁴ The lower vacancy formation energies and migration barriers in B2 suggests that a B2 shell likely allows

Li diffusion through the shell towards the unalloyed Ag interior, and Ag out diffusion through the shell to the surface where it can continue to alloy with electrochemically deposited Li. This then leads to the formation of the other Li-rich intermetallic compounds, which have exceptionally low migration barriers.

The sluggish diffusion in the FCC phase will lead to polarization and hysteresis in the voltage profile during charge and discharge.^{75,76} As a result, experimental voltage curves will differ from the equilibrium voltage curve calculated in this study (Figure 8) for typical charge and discharge rates. Measurements that are performed at low current and using small particle sizes^{10,73,74,77-79} will yield voltage curves that approach the equilibrium curve as this will allow for the electrochemical formation of the FCC solid solution.

An in-depth analysis of vacancy formation energies and migration barriers has revealed that the diffusion mechanisms in B2 LiAg are complex. Because of the topology of the B2 ordering on the BCC parent crystal structure, nearest neighbor hops necessarily lead to anti-site disorder and therefore a disruption of the thermodynamically preferred long-range order. Our DFT calculations show that nearest neighbor Li hops to the silver sublattice are unstable. A lithium can only hop to a nearest neighbor site on the Ag sublattice if it drags a second atom with it to fill the vacancy it would otherwise leave behind on the Li sublattice. These two-atom hops have surprisingly low migration barriers and likely play a significant role in mediating Li diffusion. Two atom hops are a common feature of the B2 crystal structure and has been predicted to occur in other B2 compounds such as NiAl.^{25,27,28} Second nearest neighbor hops are also viable in B2, due to its open crystal structure. While the barriers are slightly higher than nearest neighbor Ag hops or two-atom Li hops, these preserve the B2 long-range order and are more favorable from a thermodynamic point of view.

The Li-rich phases of the Li-Ag binary system, including γ_3 , γ_1 and D0₃ Li₃Ag, are all derived from BCC and have interconnected Li sublattices. They, therefore, allow for nearest neighbor Li hops without disrupting long-range order. These phases exhibit exceptionally low migration

barriers with KRA values in the range of 0.1 eV. These migration barriers are lower than those of the fastest super ion conducting solid electrolytes.^{80–84} Furthermore, they have lower vacancy formation energies on the Li sublattice than the more Ag-rich FCC and B2 phases. The Li-rich $\text{Li}_x\text{Ag}_{1-x}$ alloy should therefore enable rapid lithium diffusion. Other Li-rich intermetallics such as Li_3Sb with the D0_3 structure also exhibit very low migration barriers.⁷²

While migration barriers can provide a sense of how mobile atoms are in a particular solid, varying degrees of long and short range order and crystallographic peculiarities can cause highly correlated diffusion that lead to significant reductions in the macroscopic diffusion coefficients.^{21,23,27,29,68,69,85,86} Quantifying the effects of correlated diffusion requires numerical tools such as kinetic Monte Carlo simulations.^{44,53,67} The in-depth calculation of migration barriers and vacancy formation energies in the Li–Ag alloy system sets the stage for the calculation of room temperature diffusion coefficients using kinetic Monte Carlo simulations.

6 Conclusion

We have performed a first-principles study of the thermodynamic and kinetic properties of the Li–Ag binary system. Building on previous first-principles studies by Braga et al.¹⁷ and Xie et al.,¹⁸ we have identified two new ground states in the Li-rich portion of the phase diagram. Our analysis of the energy surface of different Li–Ag orderings at various concentrations x in $\text{Li}_x\text{Ag}_{1-x}$ along the Bain and Burgers paths have shown an unusual degree of anharmonicity. This leads to a breakdown of phonon theories within the (quasi) harmonic approximation and indicates that room temperature thermodynamic and mechanical properties should be highly temperature dependent. We have also performed a systematic investigation of migration mechanisms within the various solid solutions and intermetallic phases of the Li–Ag binary system. Vacancy formation energies are predicted to be high, leading to low concentrations of diffusion mediating vacancies. Diffusion in the FCC $\text{Li}_x\text{Ag}_{1-x}$ solid solution is pre-

dicted to be sluggish. Complex diffusion mechanisms in the B2 LiAg phase are identified, including low-barrier two-atom hops and second nearest neighbor hops. Exceptionally low migration barriers of 0.1 eV for Li hops are predicted in the Li-rich intermetallics.

7 Supporting Information

Structure enumeration details, DFT convex hull, lattice parameter changes during lithiation, optimized ground state structures in VASP POSCAR format.

8 Acknowledgements

SSB and AVDV were supported by the Defense Advanced Research Projects Agency under contract No. HR001122C0097. JT was supported by the NSF under contract No. 2311370. Use was made of computational facilities purchased with funds from the National Science Foundation (CNS-1725797) and administered by the Center for Scientific Computing (CSC). The CSC is supported by the California NanoSystems Institute and the Materials Research Science and Engineering Center (MRSEC; NSF DMR 2308708) at UC Santa Barbara. This research also used resources of the National Energy Research Scientific Computing Center (NERSC), a Department of Energy Office of Science User Facility using NERSC award BES-ERCAP0026626 and the Center for Functional Nanomaterials, Brookhaven National Laboratory, through the U.S. Department of Energy, Office of Basic Energy Sciences, contract DE-AC02-98CH10866, under award CFN312109.

References

- (1) Wang, M. J.; Kazyak, E.; Dasgupta, N. P.; Sakamoto, J. Transitioning solid-state batteries from lab to market: Linking electrochemo-mechanics with practical considerations. *Joule* **2021**, *5*, 1371–1390.
- (2) Porz, L.; Swamy, T.; Sheldon, B. W.; Rettenwander, D.; Frömling, T.; Thaman, H. L.; Berendts, S.; Uecker, R.; Carter, W. C.; Chiang, Y.-M. Mechanism of lithium metal penetration through inorganic solid electrolytes. *Advanced Energy Materials* **2017**, *7*, 1701003.
- (3) Kasemchainan, J.; Zekoll, S.; Spencer Jolly, D.; Ning, Z.; Hartley, G. O.; Marrow, J.; Bruce, P. G. Critical stripping current leads to dendrite formation on plating in lithium anode solid electrolyte cells. *Nature materials* **2019**, *18*, 1105–1111.
- (4) Kim, S.; Jung, C.; Kim, H.; Thomas-Alyea, K. E.; Yoon, G.; Kim, B.; Badding, M. E.; Song, Z.; Chang, J.; Kim, J.; others The role of interlayer chemistry in Li-metal growth through a garnet-type solid electrolyte. *Advanced Energy Materials* **2020**, *10*, 1903993.
- (5) Ning, Z.; Jolly, D. S.; Li, G.; De Meyere, R.; Pu, S. D.; Chen, Y.; Kasemchainan, J.; Ihli, J.; Gong, C.; Liu, B.; others Visualizing plating-induced cracking in lithium-anode solid-electrolyte cells. *Nature materials* **2021**, *20*, 1121–1129.
- (6) Kazyak, E.; Wang, M. J.; Lee, K.; Yadavalli, S.; Sanchez, A. J.; Thouless, M.; Sakamoto, J.; Dasgupta, N. P. Understanding the electrochemo-mechanics of Li plating in anode-free solid-state batteries with operando 3D microscopy. *Matter* **2022**, *5*, 3912–3934.
- (7) Vishnugopi, B. S.; Kazyak, E.; Lewis, J. A.; Nanda, J.; McDowell, M. T.; Dasgupta, N. P.; Mukherjee, P. P. Challenges and opportunities for fast charging of solid-state lithium metal batteries. *ACS Energy Letters* **2021**, *6*, 3734–3749.
- (8) Sanchez, A. J.; Dasgupta, N. P. Lithium Metal Anodes: Advancing our Mechanistic Understanding of Cycling Phenomena in Liquid and Solid Electrolytes. *Journal of the American Chemical Society* **2024**, *146*, 4282–4300.
- (9) Lee, Y.-G. et al. High-energy long-cycling all-solid-state lithium metal batteries enabled by silver–carbon composite anodes. *Nature Energy* **2020**, *5*, 299–308.
- (10) Spencer-Jolly, D.; Agarwal, V.; Doerrer, C.; Hu, B.; Zhang, S.; Melvin, D. L. R.; Gao, H.; Gao, X.; Adamson, P.; Magdysyuk, O. V.; Grant, P. S.; House, R. A.; Bruce, P. G. Structural changes in the silver-carbon composite anode interlayer of solid-state batteries. *Joule* **2023**, *7*, 503–514.
- (11) Okamoto, H. Supplemental Literature Review of Binary Phase Diagrams: Ag-Li, Ag-Sn, Be-Pu, C-Mn, C-Si, Ca-Li, Cd-Pu, Cr-Ti, Cr-V, Cu-Li, La-Sc, and Li-Sc. *Journal of Phase Equilibria and Diffusion* **2017**, *38*, 70–81.
- (12) Freeth, W. E.; Raynor, G. V. The constitution of the system silver-lithium. *J. Inst. Metals* **1954**, *Vol: 82*.
- (13) Pelton, A. D. The Ag- Li (Silver-Lithium) system. *Bulletin of Alloy Phase Diagrams* **1986**, *7*, 223–228.
- (14) Wang, J.; Chartrand, P.; Jung, I.-H. Thermodynamic description of the Ag-(Ca, Li, Zn) and Ca-(In, Li) binary systems. *Calphad* **2015**, *50*, 68–81.
- (15) Arnberg, L.; Westman, S.; Tucker, E. E.; Songstad, J.; Svensson, S. Note on the Structure of the Gamma Brass Like γ_3 Phase in the Silver Lithium System. *Acta Chemica Scandinavica* **1972**, *26*, 1748–1750.
- (16) Noritake, T.; Aoki, M.; Towata, S.-i.; Takeuchi, T.; Mizutani, U. Structure determination of structurally complex $\text{Ag}_{36}\text{Li}_{64}$ gamma-brass. *Acta Crystallographica Section B: Structural Science* **2007**, *63*, 726–734.

- (17) Braga, M. H.; Dębski, A.; Terlicka, S.; Gąsior, W.; Góral, A. Experimental and ab initio study of the Ag–Li system for energy storage and high-temperature solders. *Journal of Alloys and Compounds* **2020**, *817*, 152811.
- (18) Xie, F.; Diallo, M. S.; Kim, H.; Tu, Q. H.; Ceder, G. The Microscopic Mechanism of Lithiation and Delithiation in the Ag/C Buffer Layer for Anode-Free Solid-State Batteries. *Advanced Energy Materials* **2024**, *14*, 2302960.
- (19) Pavlyuk, V. V.; Dmytriv, G. S.; Tarasiuk, I. I.; Chumak, I. V.; Pauly, H.; Ehrenberg, H. Polymorphism of LiAg. *Solid State Sciences* **2010**, *12*, 274–280.
- (20) Balluffi, R. W.; Allen, S. M.; Carter, W. C. *Kinetics of materials*; John Wiley & Sons, 2005.
- (21) Van der Ven, A.; Yu, H.-C.; Ceder, G.; Thornton, K. Vacancy mediated substitutional diffusion in binary crystalline solids. *Progress in Materials Science* **2010**, *55*, 61–105.
- (22) Belak, A. A.; Van der Ven, A. Effect of disorder on the dilute equilibrium vacancy concentrations of multicomponent crystalline solids. *Physical Review B* **2015**, *91*, 224109.
- (23) Goiri, J. G.; Kolli, S. K.; Van der Ven, A. Role of short-and long-range ordering on diffusion in Ni–Al alloys. *Physical Review Materials* **2019**, *3*, 093402.
- (24) Divinski, S.; Herzig, C. On the six-jump cycle mechanism of self-diffusion in NiAl. *Intermetallics* **2000**, *8*, 1357–1368.
- (25) Mishin, Y.; Lozovoi, A.; Alavi, A. Evaluation of diffusion mechanisms in NiAl by embedded-atom and first-principles calculations. *Physical Review B* **2003**, *67*, 014201.
- (26) Herzig, C.; Divinski, S. Essentials in diffusion behavior of nickel-and titanium-aluminides. *Intermetallics* **2004**, *12*, 993–1003.
- (27) Xu, Q.; Van der Ven, A. Atomic transport in ordered compounds mediated by local disorder: Diffusion in B₂–Ni_xAl_{1–x}. *Physical Review B* **2010**, *81*, 064303.
- (28) Xu, Q.; Van der Ven, A. First-principles investigation of migration barriers and point defect complexes in B₂–NiAl. *Intermetallics* **2009**, *17*, 319–329.
- (29) Van der Ven, A.; Ceder, G. First principles calculation of the interdiffusion coefficient in binary alloys. *Physical review letters* **2005**, *94*, 045901.
- (30) Ackland, G. J.; Dunuwille, M.; Martinez-Canales, M.; Loa, I.; Zhang, R.; Sinogeikin, S.; Cai, W.; Deemyad, S. Quantum and isotope effects in lithium metal. *Science* **2017**, *356*, 1254–1259.
- (31) Natarajan, A. R.; der Ven, A. V. Toward an Understanding of Deformation Mechanisms in Metallic Lithium and Sodium from First-Principles. *Chemistry of Materials* **2019**, *31*, 8222–8229.
- (32) Behara, S. S.; Thomas, J.; Van der Ven, A. Fundamental Thermodynamic, Kinetic, and Mechanical Properties of Lithium and Its Alloys. *Chemistry of Materials* **2024**, *36*, 7370–7387.
- (33) Kresse, G.; Furthmüller, J. Efficiency of ab-initio total energy calculations for metals and semiconductors using a plane-wave basis set. *Computational materials science* **1996**, *6*, 15–50.
- (34) Kresse, G.; Furthmüller, J. Efficient iterative schemes for ab initio total-energy calculations using a plane-wave basis set. *Physical review B* **1996**, *54*, 11169.
- (35) Kresse, G.; Joubert, D. From ultrasoft pseudopotentials to the projector augmented-wave method. *Physical Review B* **1999**, *59*, 1758–1775.
- (36) Perdew, J. P.; Burke, K.; Ernzerhof, M. Generalized gradient approximation made simple. *Physical review letters* **1996**, *77*, 3865.
- (37) Blöchl, P. E. Projector augmented-wave method. *Physical Review B* **1994**, *50*, 17953–17979.

- (38) Henkelman, G.; Uberuaga, B. P.; Jónsson, H. A climbing image nudged elastic band method for finding saddle points and minimum energy paths. *The Journal of Chemical Physics* **2000**, *113*, 9901–9904.
- (39) Sheppard, D.; Terrell, R.; Henkelman, G. Optimization methods for finding minimum energy paths. *The Journal of chemical physics* **2008**, *128*.
- (40) Puchala, B.; Thomas, J. C.; Natarajan, A. R.; Goiri, J. G.; Behara, S. S.; Kaufman, J. L.; Van der Ven, A. CASM — A software package for first-principles based study of multi-component crystalline solids. *Computational Materials Science* **2023**, *217*, 111897.
- (41) Van der Ven, A.; Thomas, J. C.; Puchala, B.; Natarajan, A. R. First-principles statistical mechanics of multicomponent crystals. *Annual Review of Materials Research* **2018**, *48*, 27–55.
- (42) Thomas, J. C.; Ven, A. V. d. Finite-temperature properties of strongly anharmonic and mechanically unstable crystal phases from first principles. *Physical Review B* **2013**, *88*, 214111.
- (43) Puchala, B.; Van der Ven, A. Thermodynamics of the Zr-O system from first-principles calculations. *Physical review B* **2013**, *88*, 094108.
- (44) Puchala, B.; Thomas, J. C.; der Ven, A. V. CASM Monte Carlo: Calculations of the thermodynamic and kinetic properties of complex multicomponent crystals. arXiv preprint arXiv:2309.11761, 21 September 2023; <https://arxiv.org/abs/2309.11761>, Accessed 2024-08-09.
- (45) Bradley, A. J.; Thewlis, J.; Bragg, W. L. The structure of γ -brass. *Proceedings of the Royal Society of London. Series A, Containing Papers of a Mathematical and Physical Character* **1926**, *112*, 678–692.
- (46) Pankova, A. A.; Blatov, V. A.; Ilyushin, G. D.; Proserpio, D. M. γ -Brass Polyhedral Core in Intermetallics: The Nanocluster Model. *Inorganic Chemistry* **2013**, *52*, 13094–13107.
- (47) Merchant, A.; Batzner, S.; Schoenholz, S. S.; Aykol, M.; Cheon, G.; Cubuk, E. D. Scaling deep learning for materials discovery. *Nature* **2023**, *624*, 80–85.
- (48) Goiri, J. G.; Van der Ven, A. Phase and structural stability in Ni-Al systems from first principles. *Physical Review B* **2016**, *94*, 094111.
- (49) Natarajan, A. R.; Dolin, P.; Van der Ven, A. Crystallography, thermodynamics and phase transitions in refractory binary alloys. *Acta Materialia* **2020**, *200*, 171–186.
- (50) Kolli, S. K.; Natarajan, A. R.; Van der Ven, A. Six new transformation pathways connecting simple crystal structures and common intermetallic crystal structures. *Acta Materialia* **2021**, *221*, 117429.
- (51) Sanchez, J. M.; Ducastelle, F.; Gratias, D. Generalized cluster description of multicomponent systems. *Physica A: Statistical Mechanics and its Applications* **1984**, *128*, 334–350.
- (52) De Fontaine, D. *Solid state physics*; Elsevier, 1994; Vol. 47; pp 33–176.
- (53) Van der Ven, A.; Deng, Z.; Banerjee, S.; Ong, S. P. Rechargeable alkali-ion battery materials: theory and computation. *Chemical reviews* **2020**, *120*, 6977–7019.
- (54) Souvatzis, P.; Eriksson, O.; Katsnelson, M.; Rudin, S. Entropy driven stabilization of energetically unstable crystal structures explained from first principles theory. *Physical Review Letters* **2008**, *100*, 095901.
- (55) Ozolins, V. First-principles calculations of free energies of unstable phases: the case of fcc W. *Physical review letters* **2009**, *102*, 065702.
- (56) Hellman, O.; Abrikosov, I. A.; Simak, S. I. Lattice dynamics of anharmonic solids from first principles. *Physical Review B* **2011**, *84*, 180301.

- (57) Monserrat, B.; Drummond, N.; Needs, R. Anharmonic vibrational properties in periodic systems: energy, electron-phonon coupling, and stress. *Physical Review B* **2013**, *87*, 144302.
- (58) Chen, M.-H.; Emly, A.; Van der Ven, A. Anharmonicity and phase stability of antiperovskite Li_3OCl . *Physical Review B* **2015**, *91*, 214306.
- (59) Tadano, T.; Tsuneyuki, S. First-principles lattice dynamics method for strongly anharmonic crystals. *Journal of the Physical Society of Japan* **2018**, *87*, 041015.
- (60) Bechtel, J. S.; Thomas, J. C.; Van der Ven, A. Finite-temperature simulation of anharmonicity and octahedral tilting transitions in halide perovskites. *Physical Review Materials* **2019**, *3*, 113605.
- (61) Hutcheon, M.; Needs, R. Structural and vibrational properties of lithium under ambient conditions within density functional theory. *Physical Review B* **2019**, *99*, 014111.
- (62) Radin, M. D.; Thomas, J. C.; Van der Ven, A. Order-disorder versus displacive transitions in Jahn-Teller active layered materials. *Physical Review Materials* **2020**, *4*, 043601.
- (63) Van der Ven, A.; Ceder, G. Vacancies in ordered and disordered binary alloys treated with the cluster expansion. *Physical Review B* **2005**, *71*, 054102.
- (64) McQuarrie, D. A. *Statistical Mechanics*; University Science Books, 2000.
- (65) Mantina, M.; Wang, Y.; Chen, L.; Liu, Z.; Wolverton, C. First principles impurity diffusion coefficients. *Acta Materialia* **2009**, *57*, 4102–4108.
- (66) Van der Ven, A.; Ceder, G.; Asta, M.; Tepeesch, P. First-principles theory of ionic diffusion with nondilute carriers. *Physical Review B* **2001**, *64*, 184307.
- (67) Bortz, A. B.; Kalos, M. H.; Lebowitz, J. L. A new algorithm for Monte Carlo simulation of Ising spin systems. *Journal of Computational Physics* **1975**, *17*, 10–18.
- (68) Bhattacharya, J.; Van der Ven, A. First-principles study of competing mechanisms of nondilute Li diffusion in spinel Li_xTiS_2 . *Physical Review B* **2011**, *83*, 144302.
- (69) Kolli, S. K.; Van der Ven, A. Elucidating the factors that cause cation diffusion shutdown in spinel-based electrodes. *Chemistry of Materials* **2021**, *33*, 6421–6432.
- (70) Shewmon, P. *Diffusion in solids*; Springer, 2016.
- (71) Kolli, S. K.; Natarajan, A. R.; Thomas, J. C.; Pollock, T. M.; Van der Ven, A. Discovering hierarchies among intermetallic crystal structures. *Physical Review Materials* **2020**, *4*, 113604.
- (72) Chang, D.; Huo, H.; Johnston, K. E.; Ménétrier, M.; Monconduit, L.; Grey, C. P.; Van der Ven, A. Elucidating the origins of phase transformation hysteresis during electrochemical cycling of Li–Sb electrodes. *Journal of Materials Chemistry A* **2015**, *3*, 18928–18943.
- (73) Jin, S.; Ye, Y.; Niu, Y.; Xu, Y.; Jin, H.; Wang, J.; Sun, Z.; Cao, A.; Wu, X.; Luo, Y.; Ji, H.; Wan, L.-J. Solid–Solution-Based Metal Alloy Phase for Highly Reversible Lithium Metal Anode. *Journal of the American Chemical Society* **2020**, *142*, 8818–8826.
- (74) Corsi, J. S.; Ng, A. K.; Huang, Y.; Detsi, E. Impact of the Gibbs–Thomson Effect on Lithium Solubility in Silver Used as an Alloy Lithium-Ion Battery Anode. *ACS Applied Energy Materials* **2022**, *5*, 4547–4555.
- (75) Van der Ven, A.; See, K. A.; Pilon, L. Hysteresis in electrochemical systems. *Battery Energy* **2022**, *1*, 20210017.
- (76) Yu, H.-C.; Ling, C.; Bhattacharya, J.; Thomas, J. C.; Thornton, K.; Van der Ven, A. Designing the next generation high capacity battery electrodes. *Energy & Environmental Science* **2014**, *7*, 1760–1768.

- (77) Taillades, G.; Sarradin, J. Silver: high performance anode for thin film lithium ion batteries. *Journal of Power Sources* **2004**, *125*, 199–205.
- (78) Wu, X.; Zhang, W.; Wu, N.; Pang, S.-S.; Ding, Y.; He, G. Structural Evolution upon Delithiation/Lithiation in Prelithiated Foil Anodes: A Case Study of AgLi Alloys with High Li Utilization and Marginal Volume Variation. *Advanced Energy Materials* **2021**, *11*, 2003082.
- (79) Lee, J. H. et al. Interfacial stabilization strategy via In-doped Ag metal coating enables a high cycle life of anode-free solid-state Li batteries. *Energy Storage Materials* **2024**, *69*, 103398.
- (80) Famprikis, T.; Canepa, P.; Dawson, J. A.; Islam, M. S.; Masquelier, C. Fundamentals of inorganic solid-state electrolytes for batteries. *Nature materials* **2019**, *18*, 1278–1291.
- (81) Wang, Y.; Richards, W. D.; Ong, S. P.; Miara, L. J.; Kim, J. C.; Mo, Y.; Ceder, G. Design principles for solid-state lithium superionic conductors. *Nature materials* **2015**, *14*, 1026–1031.
- (82) Zhou, L.; Minafra, N.; Zeier, W. G.; Nazar, L. F. Innovative approaches to Li-argyrodite solid electrolytes for all-solid-state lithium batteries. *Accounts of chemical research* **2021**, *54*, 2717–2728.
- (83) Jun, K.; Sun, Y.; Xiao, Y.; Zeng, Y.; Kim, R.; Kim, H.; Miara, L. J.; Im, D.; Wang, Y.; Ceder, G. Lithium superionic conductors with corner-sharing frameworks. *Nature materials* **2022**, *21*, 924–931.
- (84) Deng, Z.; Mishra, T. P.; Mahayoni, E.; Ma, Q.; Tieu, A. J. K.; Guillon, O.; Chotard, J.-N.; Seznec, V.; Cheetham, A. K.; Masquelier, C.; others Fundamental investigations on the sodium-ion transport properties of mixed polyanion solid-state battery electrolytes. *Nature communications* **2022**, *13*, 4470.
- (85) Van der Ven, A.; Thomas, J. C.; Xu, Q.; Swoboda, B.; Morgan, D. Nondilute diffusion from first principles: Li diffusion in Li_xTiS_2 . *Physical Review B* **2008**, *78*, 104306.
- (86) Van der Ven, A.; Bhattacharya, J.; Belak, A. A. Understanding Li diffusion in Li-intercalation compounds. *Accounts of chemical research* **2013**, *46*, 1216–1225.

TOC Graphic

